



Article

# Solution-Processed SnO<sub>2</sub> Quantum Dots for the Electron Transport Layer of Flexible and Printed Perovskite Solar Cells

Muhammad Salman Kiani <sup>1</sup>, Zhandos T. Sadirkhanov <sup>1</sup>, Alibek G. Kakimov <sup>1</sup>, Hryhorii P. Parkhomenko <sup>1</sup>, Annie Ng <sup>2</sup> and Askhat N. Jumabekov <sup>1,\*</sup>

<sup>1</sup> Department of Physics, Nazarbayev University, Nur-Sultan 010000, Kazakhstan; muhammad.kiani@nu.edu.kz (M.S.K.); zhandos.sadirkhanov@nu.edu.kz (Z.T.S.); alibek.kakimov@gmail.com (A.G.K.); hryhorii.parkhomenko@nu.edu.kz (H.P.P.)

<sup>2</sup> Department of Electrical and Computer Engineering, Nazarbayev University, Nur-Sultan 010000, Kazakhstan; annie.ng@nu.edu.kz

\* Correspondence: askhat.jumabekov@nu.edu.kz

**Abstract:** Flexible and printed perovskite solar cells (PSCs) fabricated on lightweight plastic substrates have many excellent potential applications in emerging new technologies including wearable and portable electronics, the internet of things, smart buildings, etc. To fabricate flexible and printed PSCs, all of the functional layers of devices should be processed at low temperatures. Tin oxide is one of the best metal oxide materials to employ as the electron transport layer (ETL) in PSCs. Herein, the synthesis and application of SnO<sub>2</sub> quantum dots (QDs) to prepare the ETL of flexible and printed PSCs are demonstrated. SnO<sub>2</sub> QDs are synthesized via a solvothermal method and processed to obtain aqueous and printable ETL ink solutions with different QD concentrations. PSCs are fabricated using a slot-die coating method on flexible plastic substrates. The solar cell performance and spectral response of the obtained devices are characterized using a solar simulator and an external quantum efficiency measurement system. The ETLs prepared using 2 wt% SnO<sub>2</sub> QD inks are found to produce devices with a high average power conversion efficiency (PCE) along with a 10% PCE for a champion device. The results obtained in this work provide the research community with a method to prepare fully solution-processed SnO<sub>2</sub> QD-based inks that are suitable for the deposition of SnO<sub>2</sub> ETLs for flexible and printed PSCs.

**Keywords:** perovskites; solar cells; low-temperature; solution-processed; quantum dots; electron transport layer



**Citation:** Kiani, M.S.; Sadirkhanov, Z.T.; Kakimov, A.G.; Parkhomenko, H.P.; Ng, A.; Jumabekov, A.N.

Solution-Processed SnO<sub>2</sub> Quantum Dots for the Electron Transport Layer of Flexible and Printed Perovskite Solar Cells. *Nanomaterials* **2022**, *12*, 2615. <https://doi.org/10.3390/nano12152615>

Academic Editor: Juan Francisco Sánchez Royo

Received: 10 June 2022

Accepted: 25 July 2022

Published: 29 July 2022

**Publisher's Note:** MDPI stays neutral with regard to jurisdictional claims in published maps and institutional affiliations.



**Copyright:** © 2022 by the authors. Licensee MDPI, Basel, Switzerland. This article is an open access article distributed under the terms and conditions of the Creative Commons Attribution (CC BY) license (<https://creativecommons.org/licenses/by/4.0/>).

## 1. Introduction

With the tremendous improvement in the power conversion efficiency (PCE) up to 25.7% in the matter of a decade, hybrid perovskite solar cells (PSCs) made their mark in the electronic industry [1–4]. Even though some challenges such as device stability still need to be addressed, there has been a growing interest in scaling up the PSC fabrication process. Most high-efficiency PSCs are currently manufactured using the spin-coating method because of the better control over the film thickness, quality, and reproducibility of the device functional layers as well as the possibility of applying different spin-coating techniques such as dynamic spinning, hot-casting, anti-solvent annealing, gas and vacuum-quenching, etc. [5,6]. In comparison to other solution-processed techniques, spin-coating is an easy method to fabricate high-quality perovskite films [7]. One of the main limitations of the spin-coating method is its non-scalability [8]. Hence, various scalable methods including screen printing, blade coating, inkjet printing, and slot-die coating have been developed to fabricate PSCs [9–14]. The printing methods provide an appealing strategy for large-scale and high-throughput fabrication and can help to accelerate the commercialization of PSC technology [15–18].

Slot-die coating is one of the more appealing scalable coating methods due to its ability to produce solution-processed thin films with a high uniformity across large areas, its ability to coat thin films at a higher speed, its lesser material waste, and its ability to be integrated into both sheet-to-sheet (S2S) and roll-to-roll coating (R2R) systems. This affords the fabrication of PSCs on both rigid and flexible substrates [19,20]. Flexible and printed PSCs are of high interest due to their lightweight nature, portability, and low-manufacturing cost, along with the possibility of integrating them into other technologies, which promises many potential lucrative applications of this technology in wearable electronics, the internet of things (IoT), smart buildings, the automobile industry, etc. Flexible devices can be achieved by replacing traditional glass substrates with plastic substrates, such as polyethylene terephthalate (PET) or polyethylene naphthalate (PEN), with a thin layer of transparent conducting oxide (TCO). The TCO layer is typically made of indium-doped tin oxide (ITO). However, other alternatives also exist [21–23].

To successfully fabricate flexible PSCs, the three main semiconducting device functional layers, which are the electron transport layer (ETL, n-type), the perovskite photo-absorber layer (i-type), and the hole transport layer (HTL, p-type), must be processed at temperatures below the glass transition temperature of the employed plastic substrates (usually  $< 150\text{ }^{\circ}\text{C}$ ) [24–26]. The ETL is responsible for the extraction of electrons from the perovskite photo-absorber layer and then for their efficient transportation to the TCO layer. Mostly, metal oxides such as ZnO, TiO<sub>2</sub>, or SnO<sub>2</sub> are used as ETL [27,28]. However, there are other alternatives that can be based on ternary metal oxides and organic materials (e.g., BaSnO<sub>3</sub>, Zn<sub>2</sub>SnO<sub>4</sub>, PEDOT:PSS, PEDOT:PSS:MoS<sub>2</sub>, etc.) [29,30]. By covering the surface of TCO, ETL prevents the direct contact between the TCO and perovskite layers [31]. The selection of an efficient ETL requires a material with a good optical transmittance (in the visible range), a high electron mobility, a low production cost, and the energy levels (conduction and valence band energies) that form a good type-2 junction with the energy levels of the chosen perovskite material [32]. Among all the candidates, SnO<sub>2</sub> stands out as one of the best candidates for ETL due to its wide optical band gap (3.6–4.0 eV), deep conduction band, better transparency, high electron mobility ( $\sim 240\text{ cm}^2\text{ V}^{-1}\text{ s}^{-1}$ ), long carrier diffusion length, excellent chemical stability, and ease of low-temperature preparation (via solution processing) [33–36]. Due to its solution processibility, SnO<sub>2</sub> can be printed and bring advantages such as a low production cost, flexibility, easy scalability, and additive manufacturing processes within reach [37–39].

In 2018, T. Bu et al. reported slot-die coated flexible PSCs with an ETL made of commercially available SnO<sub>2</sub> NPs (15% of colloidal dispersion in H<sub>2</sub>O, Alfa Aesar). The resultant devices, in which a mixed cation and mixed anion perovskite (Cs<sub>0.05</sub>(FA<sub>0.85</sub>MA<sub>0.15</sub>)<sub>0.95</sub>Pb(I<sub>0.85</sub>-Br<sub>0.15</sub>)<sub>3</sub>) are employed as a photoactive layer and Spiro-OMeTAD is employed as an HTL, showed PCE values around 18% [40]. In 2020, Vijayaraghavan et al. reported the use of solution-processed SnO<sub>2</sub> quantum dots as an ETL for PSCs. The ETL was prepared in an aqueous medium using DI water, SnCl<sub>2</sub>·2H<sub>2</sub>O, and thiourea as precursors. PCE values of around 13.5% have been achieved at an annealing temperature of 180 °C, and the devices are fabricated on glass substrates via the spin-coating method [41]. In 2021, Ashina et al. deposited the SnO<sub>2</sub> ETLs using a dip-coating method on glass substrates with a fluorine-doped tin oxide (FTO) layer as the TCO. The authors deposited multiple layers (1–4) of a SnO<sub>2</sub> precursor solution and achieved PCE values around 3.2%. The annealing temperature for the ETL was set to 150 °C [1]. While the aforementioned PCE values obtained with the SnO<sub>2</sub> ETLs are appreciable, the annealing temperatures used in these studies, however, are still too high from the flexible PSC fabrication perspective. In 2021, Ren et al. reported a fabrication of PSCs on glass/FTO substrates using the blade coating method, in which the ETLs of devices are made of SnO<sub>2</sub> QDs with an annealing temperature of 200 °C. The authors achieved devices with PCE values around 21.6%. The obtained devices are fabricated by using a mixed perovskite consisting of FAI:MABr:MACl:PbBr<sub>2</sub>:PbI<sub>2</sub> (molar ratio: 1.1:0.2:0.5:0.2:1.2) in DMF:DMSO solvent and by employing an air-knife for the deposition of the perovskite layer [42]. Using SnO<sub>2</sub> QDs instead of NPs provides the advantage of

having a thin, dense, and uniform film of ETL. QDs have a wider bandgap (about 4.20 eV) compared to NPs, and this enhances the optical transmittance of the resulting ETL [43]. The main issue that limits the use of SnO<sub>2</sub> ETL for flexible devices is its annealing temperature, which has been found > 150 °C, while the typical flexible substrates such as PET and PEN usually have temperature limitations in terms of their structural integrity [40,44–46]. One of the possible solutions for this could be the use of already crystalline SnO<sub>2</sub> QDs for the solution-processed deposition of SnO<sub>2</sub> ETLs. Here, the use of already crystalline SnO<sub>2</sub> QDs would not only result in crystalline SnO<sub>2</sub> ETLs but would also allow for the avoidance of the high-temperature processing step, which is crucial for devices based on plastic substrates. The low-temperature and solution-processed deposition of SnO<sub>2</sub> ETL is advantageous from the perspective of flexible and printed optoelectronics.

In this work, a method to employ SnO<sub>2</sub> quantum dots, synthesized via a solvothermal method, to prepare ETLs of flexible PSCs fabricated on PET/ITO substrates is demonstrated. For the synthesis of SnO<sub>2</sub> quantum dots, tin chloride and ethanol are used as the solute and solvents, respectively. The obtained quantum dots are crystalline with sizes ~2.4 nm [47]. The obtained SnO<sub>2</sub> QDs are used to prepare aqueous inks with different SnO<sub>2</sub> QD concentrations to slot-die coat ETLs on PET/ITO substrates with a low annealing temperature. The obtained ETLs on PET/ITO substrates are then used to fabricate flexible and printed PSCs by also using the slot-die coating method. The metallic contacts (gold electrodes) of the devices are deposited using a thermal evaporator and a shadow mask. The solar cell performances of the devices are compared to rule out the best ETL ink composition. A statistical analysis of the device performance parameters is carried out, and the performance of the champion device is discussed. The findings of this study can be useful in the synthesis and use of SnO<sub>2</sub> QDs for application in printed and flexible optoelectronics.

## 2. Materials and Methods

### 2.1. Materials

Methylammonium iodide (MAI, 99.995%) was purchased from GreatCell Solar. Tin chloride dihydrate (SnCl<sub>2</sub>·2H<sub>2</sub>O, 98%), lead iodide (PbI<sub>2</sub>, 99%), chlorobenzene (CB, 99.80%), 4-tert-Butylpyridine (4tBp, 98%), bis(trifluoromethane)sulfonimide lithium salt (Li-TFSI, 99%), acetonitrile (ACN, 99.80%), methylamine solution (MA, 33 wt% in absolute ethanol), and acetone (99.80%) were purchased from Merck. 2,2',7,7'-Tetrakis-(*N,N*-di-4-methoxyphenylamino)-9,9'-spirobifluorene (Spiro-MeOTAD, 99.50%) and potassium hydroxide pellets (KOH, 85%) were purchased from Lumtec and ACS reagent, respectively. 2-Propanol (IPA, 99.80%) and ethanol (96.3%) were purchased from a local supplier. Gold (Au, 99.99%) was purchased from Kurt. J. Lesker. All the chemicals were used as received without any treatment.

### 2.2. SnO<sub>2</sub> QDs Synthesis

SnO<sub>2</sub> QDs were prepared by dissolving 1 mol of SnCl<sub>2</sub>·2H<sub>2</sub>O in 10 mL of ethanol in the presence of oxygen. The mixture of precursors was vigorously stirred for 4 h using a magnetic stirrer. The obtained QD solution was then transferred into a 50 mL Teflon liner in a stainless-steel autoclave (Toption). The solvothermal treatment was carried out at 150 °C in an oven for 24 h [48]. After this, the obtained solution was centrifuged to precipitate the SnO<sub>2</sub> QDs. The obtained precipitate (SnO<sub>2</sub> QDs) was washed consecutively with DI water, acetone, and ethanol. Then, the SnO<sub>2</sub> QDs were dried at 80 °C in the oven for 12 h. A flow chart in Figure 1 shows the process for the synthesis of SnO<sub>2</sub> QDs to prepare SnO<sub>2</sub> QD inks.

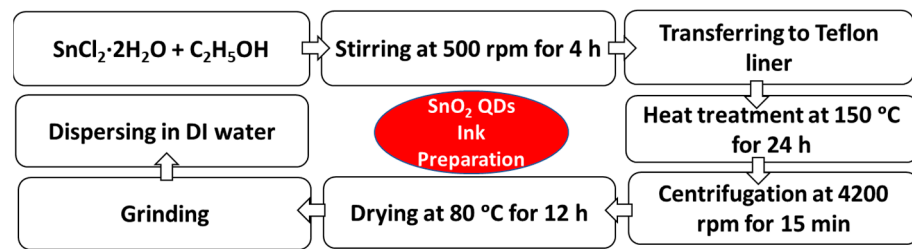


**Figure 1.** Preparation of ETL ink with SnO<sub>2</sub> QDs.

### 2.3. Ink Preparations

The aqueous SnO<sub>2</sub> QD inks were prepared using freshly synthesized SnO<sub>2</sub> QDs. For this, the dried powder of SnO<sub>2</sub> QDs was ground and redispersed in DI water (at different wt%) with the help of 1 M KOH (in water) solution as a pH mediator (see Figure 1). The obtained colloidal solution was then filtered using a 0.45 µm-sized PTFE filter and further diluted with DI water to obtain the final ink solutions, with the concentrations of SnO<sub>2</sub> QDs being 1, 1.5, 2, 2.5, and 3 wt%. The perovskite (methylammonium lead iodide, MAPbI<sub>3</sub>) ink was prepared using PbI<sub>2</sub> and MAI as precursors, while MA and ACN were used as solvents. For this, 1 mol of PbI<sub>2</sub> and MAI were dissolved in 700 µL of MA by stirring at 70 °C and 460 rpm for 1 h using a hot plate with a magnetic stirrer. Next, 700 µL of ACN was added to the solution and stirred at room temperature for an additional 3 h. The obtained final perovskite ink solution was then filtered using a 0.45 µm-sized PTFE filter and was ready for use. The HTL ink was prepared by simply dissolving 45 mg of Spiro-MeOTAD in 1 mL of CB using a vortex shaker. After 1 h of shaking, 28.8 µL 4tBp and 17.5 µL lithium salt solution (520 mg mL<sup>-1</sup> of Li-TFSI in ACN) were added to the Spiro-MeOTAD/CB solution. The final HTL ink solution was then filtered using a 0.45 µm-sized PTFE filter for further use.

### 2.4. Device Fabrication

For the fabrication of flexible and printed PSCs, a freshly cleaned PET/ITO substrate was placed onto the chuck of a slot-die coater (VectorSC, FOM Technologies, Copenhagen, Denmark) and fixed using vacuum suction to keep the substrate perfectly flat on the surface of the chuck. The PET/ITO substrates were cleaned by (1) washing them consecutively in DI detergent water, clean DI water, acetone, and IPA for 10 min in each media using an ultrasonic bath, (2) drying them with the flow of compressed air, and (3) subjecting them to UV-Ozone treatment for 10 min. The SnO<sub>2</sub> QDs inks were printed on the PET/ITO substrates using a clean slot-die head. Then, the substrates were annealed in the oven at 140 °C for 30 min. This step is necessary to remove the remaining water from the ETL film prior to the deposition of the perovskite layer on top of it. Once the substrates were cooled down to room temperature, they were placed onto the chuck of the slot-die coater again, and the perovskite ink was printed on top of the ETL using a clean slot-die head. Then, the substrates were annealed again in the oven at 100 °C for 10 min to crystallize the perovskite layer. Next, the HTL ink was printed on top of the perovskite layer using a clean slot-die head. All of the device functional layers were printed in an ambient environment at room temperature (17 °C) and a relative humidity of 20–24%. After depositing all the functional layers, the substrates were left in the atmosphere of oxygen at room temperature for 4 h (oxygen annealing). This step helps to enhance the hole transporting properties of the Spiro-MeOTAD HTL. Finally, the 80 nm-thick Au electrodes were deposited using a vacuum thermal evaporator (Mini SPECTROS, Kurt J. Lesker, USA) and a shadow mask. Overall, the devices have the following structure: PET/ITO/SnO<sub>2</sub>/MAPbI<sub>3</sub>/Spiro-MeOTAD/Au. Figure 2 represents a schematic diagram of the device fabrication process and an energy level diagram for the fabricated PSCs [49,50]. The reference devices without ETL were also fabricated using the exact same steps as those in the regular devices (with ETL), except for the ETL deposition step, which was omitted. Hence, the reference devices have the following structure: PET/ITO/MAPbI<sub>3</sub>/Spiro-MeOTAD/Au.

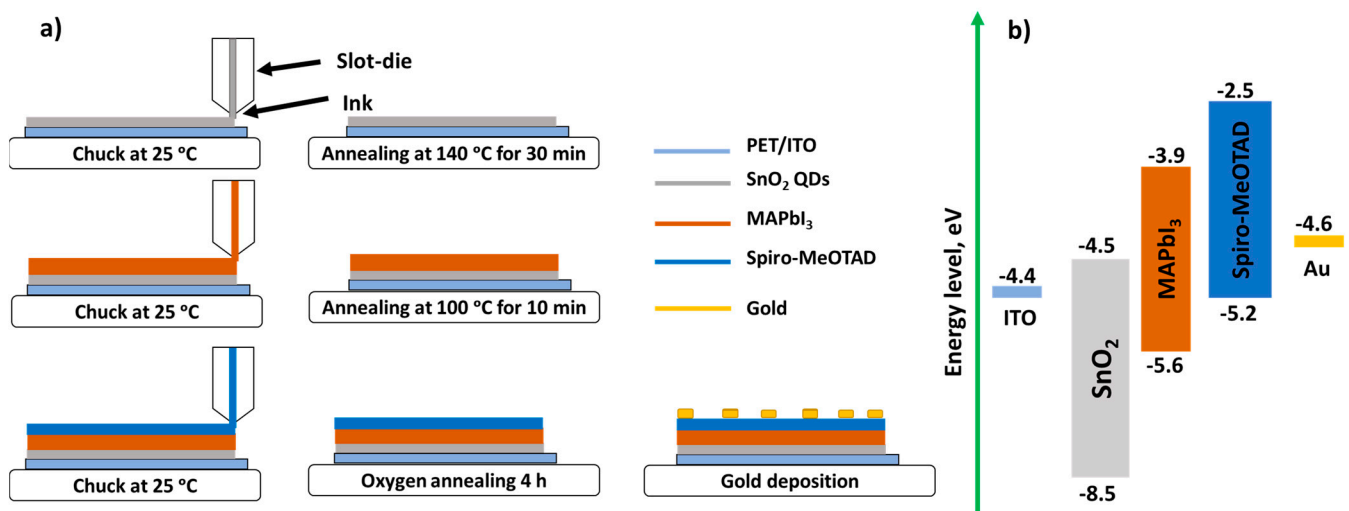


**Figure 2.** (a) Schematic diagram of the device fabrication process. (b) Energy level diagram for PSCs.

### 2.5. Characterization

A transmission electron microscope (TEM, JEOL JEM - 1400 Plus, Tokyo, Japan) was used to estimate the particle size and crystallinity of the obtained SnO<sub>2</sub> QDs. An X-ray diffractometer (XRD, SmartLab Rigaku, Austin, TX, USA) was used to examine the crystal structure of the SnO<sub>2</sub> QDs (using Cu K $\alpha$  = 1.5418 Å). A scanning electron microscope (SEM, Zeiss Crossbeam 540, Oberkochen, Germany) was used to obtain the cross-section images of the fabricated devices and to study the morphology of the prepared ETLs. The optical transmittance of the samples was measured using a UV-Vis spectrometer (Lambda 1050, PerkinElmer, Waltham, MA, USA). The performance of the fabricated devices was characterized using a solar simulator (Oriel Sol3A, Newport, Irvine, CA, USA) and a Keithley 2400 source (Keithley, Solon, Ohio, USA). The current density-voltage ( $J$ - $V$ ) curves of the devices were recorded at a scan rate of 400 mV s<sup>-1</sup> between -0.2 V and +1.2 V. The device area was 0.1 cm<sup>2</sup>, and a mask with an active area of 0.03 cm<sup>2</sup> was used to measure the device  $J$ - $V$  curves. An external quantum efficiency (EQE) measurements system (ORIEL IQE-200, Newport, Irvine, CA, USA) was used to record the EQE spectra of the devices.

## 3. Results and Discussion

### 3.1. Crystallinity of SnO<sub>2</sub> QDs

The XRD measurements were performed on as-prepared SnO<sub>2</sub> QDs to analyze their structure. Figure 3 shows an XRD pattern of as-prepared SnO<sub>2</sub> QDs. The XRD pattern shows the diffraction peaks at  $2\theta = 26.7^\circ$ ,  $34.05^\circ$ ,  $38.24^\circ$ ,  $52.1^\circ$ ,  $58.07^\circ$ ,  $62.5^\circ$ , and  $65.00^\circ$ , which correspond to the reflections from the (110), (101), (200), (211), (002), and (301) lattice planes of SnO<sub>2</sub>, respectively. All of the peaks match well with JCPDS Data Card No. 77-0452, indicating that the current structure is for SnO<sub>2</sub>, which exists in the tetragonal rutile crystalline phase. The crystal lattice parameters were calculated to be  $a = 0.4739$  nm and  $c = 0.3221$  nm (JCPDS card # 77-0452) [51–53]. The estimated average crystallite size for the SnO<sub>2</sub> QDs is around 2.4 nm, which was calculated from the two major peaks at (110) and (211) using Scherrer's equation (see Supporting Information) [38,39]. The full width at half-maximum (FWHM) values for the (110) and (211) peaks are about  $3.6^\circ$  and  $3.5^\circ$ , respectively.

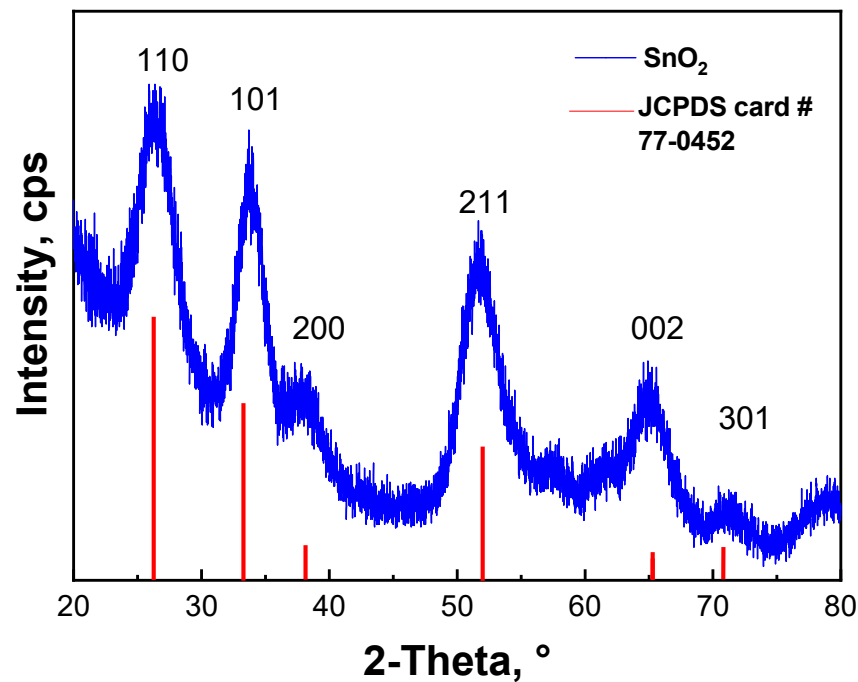


**Figure 3.** XRD pattern of as-prepared SnO<sub>2</sub> QDs.

### 3.2. Transmission Electron Microscopy

A TEM analysis is conducted to obtain the electron micrographs of as-prepared SnO<sub>2</sub> QDs and to estimate their particle size. The average particle size estimated from the TEM images (see Figure 4 and Figure S1 in Supporting Information) is around 2.4 nm, which is in good agreement with the crystallite size determined using the XRD data shown in Figure 3 [48]. The TEM image also indicates that the prepared particles have a uniform size distribution (Figure S1 in Supporting Information) and a crystalline structure, which is evident from the fringes shown in Figure 4b. The estimated value of d-spacing from the TEM image of the as-prepared SnO<sub>2</sub> QDs is around 0.33 nm (see the inset image in Figure 4b). This corresponds to the {110} planes of SnO<sub>2</sub>. Since the size of the prepared SnO<sub>2</sub> QDs is smaller than the Bohr exciton radius (around 2.7 nm), it is reasonable to state that the prepared particles are QDs of SnO<sub>2</sub> [48,54].

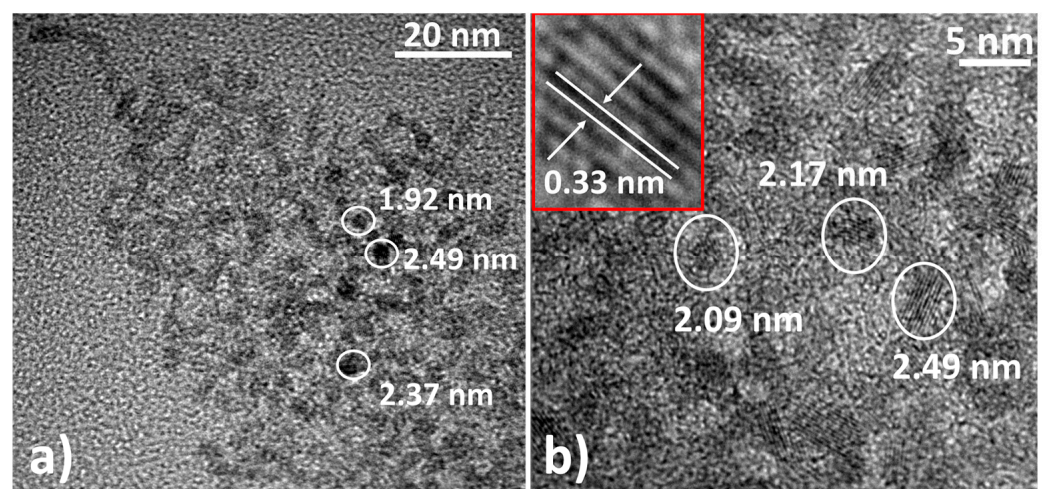


**Figure 4.** TEM micrographs of SnO<sub>2</sub> QDs synthesized via a solvothermal route at a magnification of (a) 40 kX and (b) 1500 kX. The inset image in (b) shows the fringes and d-spacing of SnO<sub>2</sub> QDs.

### 3.3. Optical Analysis

The investigation of the optical properties of the ETLs prepared using SnO<sub>2</sub> inks with different SnO<sub>2</sub> QD concentrations was carried out using a UV-Vis spectrometer. Figure 5 shows the measured transmittance spectra of the slot-die coated ETLs on glass substrates for the 250–900 nm wavelength range. A comparison of the UV-Vis spectra for different ETLs shows that the transmittance of the ETL made with a 1 wt% SnO<sub>2</sub> QD ink is the highest and is well above 90% throughout the entire visible spectrum. The second highest transmittance is for the ETL made with a 2 wt% SnO<sub>2</sub> QD ink, which is slightly higher than the one made with a 1.5 wt% SnO<sub>2</sub> QD ink. The UV-Vis transmittance of the ETL made with a 3 wt% SnO<sub>2</sub> QD ink is slightly lower than the one made with the 1.5 wt% SnO<sub>2</sub> QD ink. The lowest transmittance is observed for the ETL made with a 2.5 wt% SnO<sub>2</sub> QD ink. Overall, the UV-Vis transmittance measurements for the ETLs made with the 1, 2, and 3 wt% SnO<sub>2</sub> QD inks show that, with an increase in the concentration of SnO<sub>2</sub> QDs in the inks, the obtained ETL films become thicker. This is expected, since inks with a higher SnO<sub>2</sub> QD content should produce thicker films. The observed minor inconsistencies with the ETLs made with the 1.5 and 2.5 wt% SnO<sub>2</sub> QD inks could be associated with some small deviations in the ink preparation and deposition steps, which may influence the thickness of the resulting films. It is noteworthy to point out that the transmittance of all the ETLs is above 90%, which is beneficial from the PSC device perspective. Such high light transmittances of the obtained ETLs allow more photons to pass into the perovskite layer and enable the generation of more charge carriers in the complete devices [55–58].

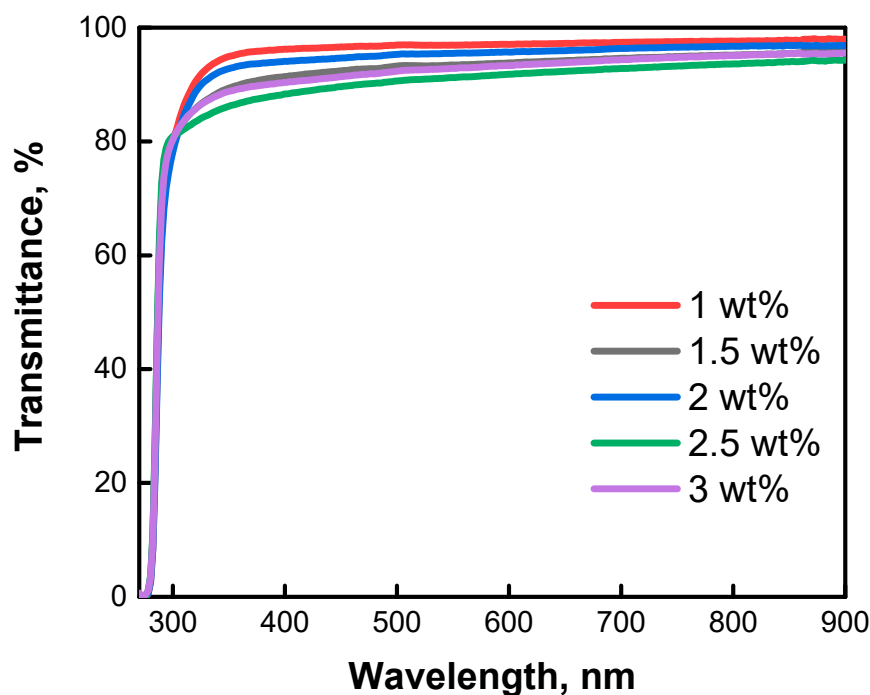


**Figure 5.** UV-Vis transmittance spectra of ETLs on glass substrates prepared using ETL inks with different SnO<sub>2</sub> QD concentrations.

### 3.4. Scanning Electron Microscopy

The SEM imaging is used to determine the thickness of the device functional layers. Figure 6a shows the cross-section of an ETL on glass/FTO made using a 2 wt% SnO<sub>2</sub> QD ink. The thickness of the SnO<sub>2</sub> QD ETL is about 25 nm. The cross-section SEM images of ETLs made using the 1, 1.5, 2.5, and 3 wt% SnO<sub>2</sub> QD inks are shown in Figure S2 in Supporting Information. Figure 6b shows all three functional layers of a PSC slot-die coated on glass/FTO. Here, the ETL is about 21–25 nm thick (see inset image), while the MAPbI<sub>3</sub> and the HTL have thicknesses of around 600 and 650 nm, respectively. Figure 6c shows

a top view SEM image of a bare PET/ITO substrate, in which the crystallites of the ITO layer are clearly visible. Figure 6d shows the top view SEM image of a 2 wt% SnO<sub>2</sub> QD ETL slot-die coated on a PET/ITO substrate. The image indicates that the layer of SnO<sub>2</sub> QDs completely covers the surface of the PET/ITO substrate, as no visible pinholes can be observed from the ETL through which the surface of the ITO can be seen. By comparing Figure 6c,d, the SnO<sub>2</sub> QD ETL prepared by our technique can uniformly cover the surface of the PET/ITO substrate. A uniform coverage of the TCO layer by an ETL is necessary for good device operation.

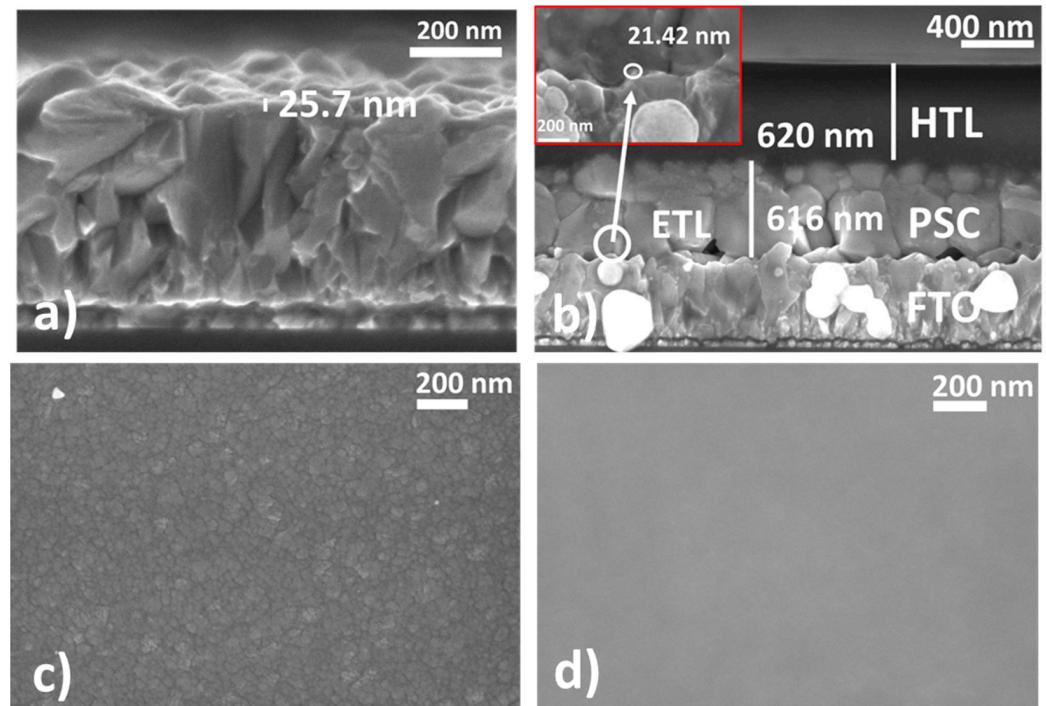


**Figure 6.** (a) SEM cross-section view of the ETL with SnO<sub>2</sub> QDs on glass/FTO. (b) SEM cross-section view of slot-die coated device functional layers on glass/FTO (inset shows the presence of ETL between the FTO and perovskite layers). (c) SEM top view image of the PET/ITO substrate (magnification at 100 kX). (d) SEM top view image of the SnO<sub>2</sub> QD ETL on the PET/ITO substrate (magnification at 100 kX).

### 3.5. Device Analysis

Flexible and printed PSCs on PET/ITO substrates without and with ETLs, prepared using SnO<sub>2</sub> QD solutions with different concentrations (0, 1, 1.5, 2, 2.5, and 3 wt%), were fabricated to rule out the suitable concentration of SnO<sub>2</sub> QDs in the ETL inks. For this, devices are fabricated for each concentration of SnO<sub>2</sub> QDs in the ETL inks. Hereon, the ETLs prepared with SnO<sub>2</sub> QDs with 0, 1, 1.5, 2, 2.5, and 3 wt% will be referred to as E0, E1, E2, E3, E4, and E5, respectively. It should be noted that E0 refers to bare ITO. The prepared devices are tested, and a statistical analysis of the performance parameters of the top 40 well-performing devices for different ETLs (E0, E1, E2, E3, E4, and E5) is carried out.

Figure 7 shows the statistical data for the solar cell parameters (obtained from the reverse scans) such as open-circuit voltage ( $V_{oc}$ ), short-circuit current density ( $J_{sc}$ ), fill factor (FF), PCE, series resistances ( $R_s$ ), and shunt resistances ( $R_{sh}$ ) presented for devices with E0, E1, E2, E3, E4, and E5 ETLs. Figure 7a shows that the average  $J_{sc}$  values increase from E0 to E4. For E0, the  $J_{sc}$  value is around  $1.12 \text{ mA cm}^{-2}$ , which, for E1, increases up to  $7.7 \text{ mA cm}^{-2}$ . For E2, the  $J_{sc}$  value is  $12.95 \text{ mA cm}^{-2}$ , which is higher than that in E1 by around 40%. The average  $J_{sc}$  value for E3 ( $13.28 \text{ mA cm}^{-2}$ ) is only slightly higher than that in E2. The average  $J_{sc}$  value of E4 is about  $14.31 \text{ mA cm}^{-2}$ , which is the highest among the compared devices. As for E5, there is a small drop in the average  $J_{sc}$  value as compared to

E4. Figure 7b shows that there is also a continuous increase in the average  $V_{oc}$  values from E0 to E3. The average  $V_{oc}$  value in E3 is around 0.93 V, which is  $\sim 2.5$  times higher than that in E0 and  $\sim 13\%$  higher than that in E1. Afterwards, a continuous decrease in the average  $V_{oc}$  values was observed for the devices with higher concentrations of SnO<sub>2</sub> QDs in the ETL inks (E4 and E5).

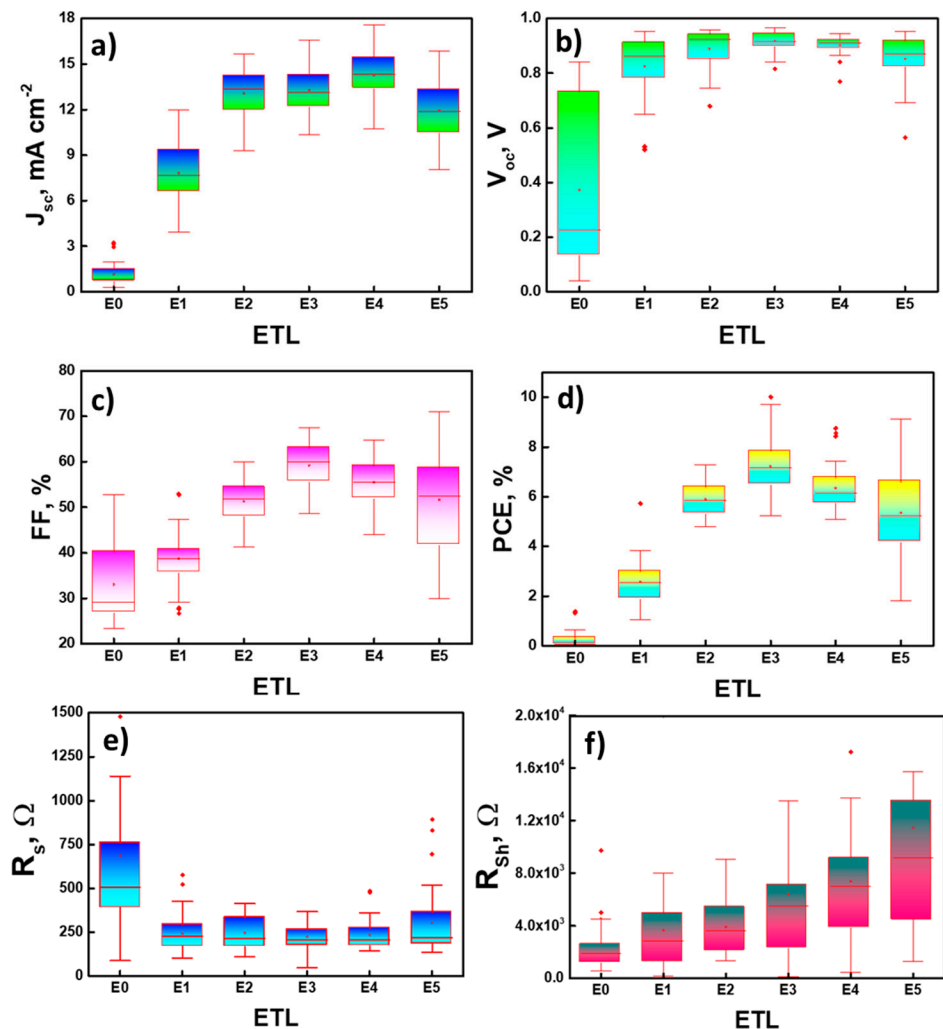


**Figure 7.** Comparison of the average values of (a)  $J_{sc}$ , (b)  $V_{oc}$ , (c) FF, (d) PCE, (e)  $R_s$ , and (f)  $R_{sh}$  of printed and flexible PSCs for different SnO<sub>2</sub> ETLs prepared using SnO<sub>2</sub> QD inks with different QD concentrations.

The observed variations of the  $V_{oc}$  and  $J_{sc}$  values with the change in the concentration of SnO<sub>2</sub> QDs in the ETL inks might be due to the impact of the ETL morphology and thickness on the carrier recombination processes and series resistance in the devices (see Table 1) [59]. With an increase in the concentration of SnO<sub>2</sub> QDs in the ETL ink, the resulting devices show higher  $R_s$  values, as depicted in Figure 7e. The increase in  $R_{sh}$  values with an increase in the concentration of SnO<sub>2</sub> QDs in the ETL inks (see Figure 7f) might indicate that the resulting ETL becomes more compact and has fewer pinholes. This helps to reduce charge carrier back-reaction, which is possibly the reason for the initial increase in the average  $V_{oc}$  and  $J_{sc}$  values (E0 to E3). The following decrease in the average  $J_{sc}$  value in E5 might originate from the suboptimal thickness of the ETL, which decreases the transmission of photons through the ETL (see Figure 5). As for the average  $V_{oc}$  values in E4 and E5, it might be due to the higher charge recombination at the ETL/perovskite interface due to

high the  $R_S$  in the devices and the lower transmittance of the ETL films as compared to E3 [60].

**Table 1.** Statistical analysis of the performance parameters of the top 40 well-performing devices for different ETLs.

ETLs.	Scan Direction	$J_{sc}$ , $\text{mA cm}^{-2}$	$V_{oc}$ , V	FF, %	PCE, %	$R_S$ , $\Omega$	$R_{Sh}$ , $\text{k}\Omega$
E0 (ref.)	Reverse	$1.15 \pm 0.113$	$0.37 \pm 0.046$	$33.06 \pm 1.326$	$0.21 \pm 0.050$	$689.6 \pm 119$	$4.6 \pm 2.4$
	Forward	$0.94 \pm 0.102$	$0.33 \pm 0.048$	$27.95 \pm 0.484$	$0.12 \pm 0.027$	$994.8 \pm 252.2$	$16.6 \pm 10.4$
E1 (1 wt%)	Reverse	$7.72 \pm 0.293$	$0.82 \pm 0.017$	$38.69 \pm 0.849$	$2.52 \pm 0.164$	$238.4 \pm 16.6$	$3.7 \pm 0.5$
	Forward	$5.56 \pm 0.264$	$0.72 \pm 0.021$	$28.85 \pm 0.723$	$1.19 \pm 0.096$	$447.8 \pm 121.1$	$3.9 \pm 0.4$
E2 (1.5 wt%)	Reverse	$12.95 \pm 0.491$	$0.89 \pm 0.013$	$51.15 \pm 1.576$	$5.84 \pm 0.338$	$246.6 \pm 14.1$	$3.9 \pm 0.3$
	Forward	$10.08 \pm 0.572$	$0.82 \pm 0.014$	$36.29 \pm 1.453$	$2.99 \pm 0.23$	$230.7 \pm 11.4$	$3.7 \pm 0.3$
E3 (2 wt%)	Reverse	$13.28 \pm 0.22$	$0.93 \pm 0.01$	$59.22 \pm 0.75$	$7.23 \pm 0.18$	$222.7 \pm 11.2$	$6.3 \pm 1.4$
	Forward	$8.52 \pm 0.35$	$0.88 \pm 0.01$	$28.27 \pm 0.97$	$2.15 \pm 0.12$	$221.3 \pm 10.3$	$3.3 \pm 0.3$
E4 (2.5 wt%)	Reverse	$14.31 \pm 0.63$	$0.92 \pm 0.01$	$53.10 \pm 1.82$	$6.98 \pm 0.46$	$232.6 \pm 12.9$	$7.4 \pm 1.1$
	Forward	$10.34 \pm 0.64$	$0.85 \pm 0.01$	$32.50 \pm 1.44$	$3.08 \pm 0.32$	$223.5 \pm 15.4$	$4.2 \pm 0.4$
E5 (3 wt%)	Reverse	$11.76 \pm 0.30$	$0.83 \pm 0.02$	$50.62 \pm 1.90$	$5.16 \pm 0.31$	$297.2 \pm 28.6$	$11.7 \pm 1.7$
	Forward	$7.52 \pm 0.30$	$0.75 \pm 0.02$	$25.41 \pm 0.77$	$1.50 \pm 0.12$	$271.0 \pm 27.4$	$5.4 \pm 0.8$

Statistically, E3 ETL is found to be the most suitable to obtain well-performing devices. It is also noteworthy that the highest performing device (champion device) is also obtained using E3 ETLs. Figure 8a shows the  $J$ - $V$  curves of the champion device with E3 ETL. The  $V_{oc}$ ,  $J_{sc}$ , and FF of the champion device for the reverse scan are around 0.96 V, 17  $\text{mA cm}^{-2}$ , and 63%, respectively. This results in a device PCE of around 10%. The solar cell parameters obtained from both the forward and reverse  $J$ - $V$  scan directions are presented in Table 2. The  $J$ - $V$  curves of the ‘champion devices’ with E0, E1, E2, E4, and E5 ETLs and the corresponding solar cell parameters are presented in Figure S3 in Supporting Information.

**Table 2.** Solar cell performance parameters for the champion device.

Scan Direction	$J_{sc}$ , $\text{mA cm}^{-2}$	$V_{oc}$ , V	FF, %	PCE, %	Integrated $J_{sc}$ , $\text{mA cm}^{-2}$
Reverse	16.6	0.958	62.9	10.006	10.76
Forward	12.3	0.925	25.4	2.906	

Figure 7c depicts that there is a steep increase in the average FF values from E0 to E3, followed by a slow decrease for E4 and E5. This trend is somewhat similar to the ones observed in  $V_{oc}$  and  $J_{sc}$ . The average FF value has a remarkable increase of around 37% when the  $\text{SnO}_2$  QD concentration in the ETL ink is doubled (from 1 wt% (E1) to 2 wt% (E3)). Generally, FF is a complex phenomenon. It depends on many device parameters and processes taking place in solar cells. Here, the initial increase in the average FF values from E0 to E3 could be associated with a decrease in the charge carrier recombination and, possibly, an increase in the electrical conductivity of the ETLs due to an increase in their thickness [61–63]. For E4 and E5, the decrease in FF might be due to an increase in  $R_S$  in the devices [60].

The trends in the  $V_{oc}$ ,  $J_{sc}$ , and FF values determine the final trend for the overall variation of the average PCE with the change in the concentration of  $\text{SnO}_2$  QDs in the ETL inks. As expected and consistent with the variations in the average values of  $V_{oc}$ , FF, and, to a certain extent,  $J_{sc}$ , the average PCE values of the devices increase from E0 to E3 and then decrease. The average PCE in E3 is almost three times higher than that in E1. This is mostly due to the significant increases in the average  $J_{sc}$  (by a factor of  $\sim 1.8$ ) and FF (by a factor of  $\sim 1.5$ ) values when the  $\text{SnO}_2$  QD concentration in the ETL ink is doubled (from 1 wt% (E1) to 2 wt% (E3)). All the devices with ETLs (E1, E2, E3, E4, and E5) have significantly higher performances compared to the devices without any ETL (E0). This indicates the necessity of ETLs to obtain a good performance of PSC devices. A detailed overview of the solar cell parameters is presented in Table 1. We note that most of the metal

oxide (e.g., ZnO, SnO<sub>2</sub>, and NiO) inks that are commercially available and used in printed optoelectronic devices also have a metal oxide solid content at around 2–2.5 wt%. In light of this, the trends observed in this work appear reasonable and somewhat consistent with the commercially available inks [64–67].

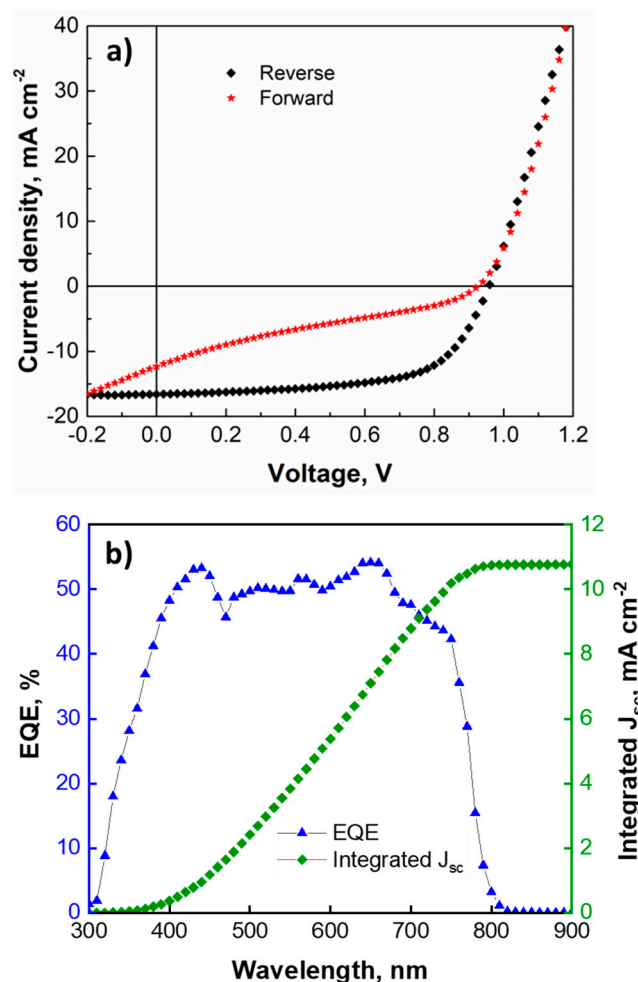


**Figure 8.** (a)  $J$ - $V$  curves and (b) EQE spectrum with an integrated  $J_{sc}$  curve for the champion device.

The external quantum efficiency (EQE) measurements are also performed on the champion device with E3 ETL to obtain its spectral response. Figure 8b shows that the device has an EQE spectrum that is typical for the MAPbI<sub>3</sub>-based PSCs [68,69]. The device shows more or less stable EQE values at around 50% throughout the visible spectrum. The integrated  $J_{sc}$  value obtained from the EQE spectrum of the champion device is around 11 mA cm<sup>-2</sup> (Figure 8b). This is comparable to the  $J_{sc}$  value of the device extracted from the  $J$ - $V$  curve for the forward scan direction (see Table 2). The EQE spectra of the 'champion devices' with E0, E1, E2, E4, and E5 ETLs are presented in Figure S4 in Supporting Information.

In order to study the mechanical stability of flexible PSCs, the fabricated device with E3 ETLs is subjected to a repeated cycle of compressive bending to a radius of around 1 cm, and their solar cell performance is measured after every 10 bending cycles. Overall, the devices are subjected to 50 bending cycles. Figure 9 shows the variations in the solar cell parameters of a device with E3 ETL upon bending. After the first 10 bending cycles, the  $J_{sc}$  value of the device decreases by 45%, and the FF value decreases by 37%. These fast decays in the  $J_{sc}$  and FF values after the first 10 bending cycles could mainly be associated with the deterioration of the structural integrity of the device due to the appearance of cracks in the ITO layer [70–74]. This significantly increases the device series resistance. Between the 10th and 50th bending cycles, the FF value of the device decays rather slowly

and monotonously. A somewhat similar but slightly faster decay of the device's  $J_{sc}$  value is observed for the same bending cycle range. These decays could be due to the further and more complex deterioration (e.g., micro-delamination of the device functional layers, formation of micro-cracks and micro-voids in the device's functional layers, etc.) of the device's structural integrity [75–77]. As for the device's  $V_{oc}$ , there is almost a linear decay trend with the increase in the number of bending cycles. This indicates the formation of many defects (microcracks) in the perovskite layer, which increases the rate of charge carrier recombination in the layer and leads to a corresponding decrease in the  $V_{oc}$  and  $J_{sc}$  values of the devices [78–81]. These trends in the behavior of the  $J_{sc}$ , FF, and  $V_{oc}$  during the bending test result in a fast decay of the device's PCE after the first 10 bending cycles (a decrease from 7% to 2.5%) and a slower decay between the 10th and 50th bending cycles. After the 50th bending cycle, the PCE of the device becomes around 0.84%. This is smaller (by a factor of ~8) than the initial PCE value (7%) of the device. The mechanical stability could be further improved by the modification of the functional layers and their interfaces in PSCs as well as the application of more durable TCO layers [82].

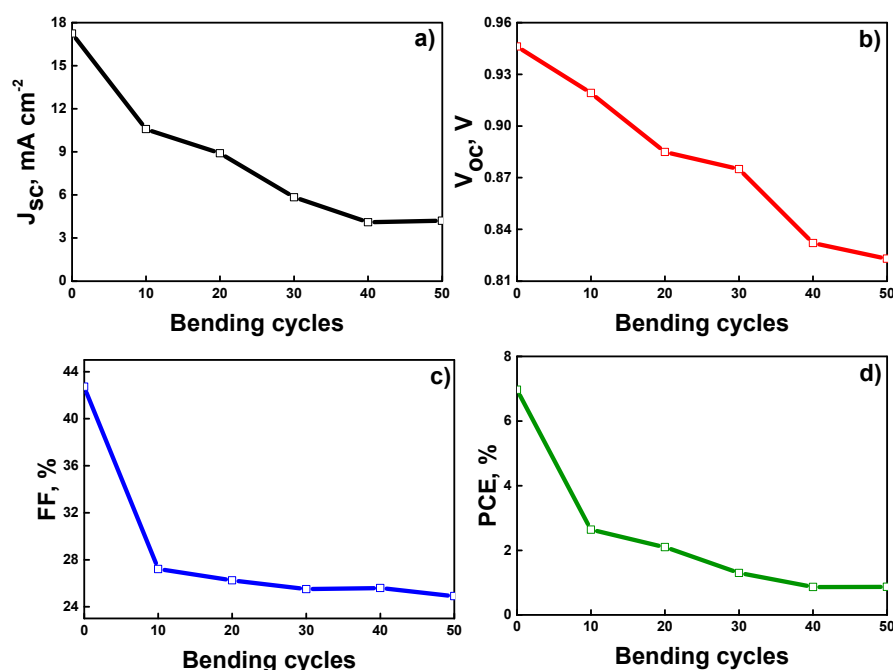


Figure 9. Variation in the (a)  $J_{sc}$ , (b)  $V_{oc}$ , (c) FF, and (d) PCE of the device upon bending.

#### 4. Conclusions

In summary, the synthesis and application of  $\text{SnO}_2$  QDs as ETLs for flexible and printed PSCs based on PET/ITO substrates are demonstrated.  $\text{SnO}_2$  QDs with diameters around 2.4 nm are obtained using a solvothermal synthesis method. The QDs of  $\text{SnO}_2$  in the prepared inks are crystalline and well-dispersed. The device functional layers (ETL, perovskite, and HTL) are deposited using a slot-die coating method under ambient air conditions. In order to optimize the printed PSCs, the water-based inks with different  $\text{SnO}_2$  QD concentrations for preparing different thicknesses of ETLs are investigated. The devices with ETLs obtained by using a 2 wt%  $\text{SnO}_2$  QD ink show the best performance (the average PCE for the reverse scan direction is around 7.23%). The champion device, which shows a PCE value of around 10%, is also obtained with the ETL prepared using the 2 wt%  $\text{SnO}_2$  QD ink. The mechanical stability of a device with the 2 wt%  $\text{SnO}_2$  QD ETL is investigated by subjecting the device to a bending test. The initial fast degradation of the performance of the device is attributed to the cracking of the ITO layer in the device, whereas the further slower decay is a result of more complex deterioration in the structure of the device. The findings of the work can be useful in developing new electronic inks for optoelectronic

applications and in establishing the advanced low-temperature manufacturing protocols for the printing of optoelectronic devices on heat-sensitive substrates.

**Supplementary Materials:** The following supporting information can be downloaded at: <https://www.mdpi.com/article/10.3390/nano12152615/s1>, Figure S1. Particle size distribution; Figure S2. SEM cross-section images of ETLs on glass/FTO made with (a) 1 wt%, (b) 1.5 wt%, (c) 2.5 wt% and, (d) 3 wt% of SnO<sub>2</sub> QD inks; Figure S3. J-V curves of champion devices with (a) E0, (b) E1, (c) E2, (d) E4, and (e) E5 ETLs; Figure S4. EQE spectra of champion devices with different ETLs (E0, E1, E2, E4, and E5) [83,84].

**Author Contributions:** Conceptualization, A.N.J.; data curation, M.S.K.; formal analysis, A.N.J.; investigation, M.S.K., Z.T.S., A.G.K. and H.P.P.; methodology, M.S.K., Z.T.S., A.G.K., H.P.P. and A.N.J.; resources, A.N. and A.N.J.; supervision, A.N.J.; visualization, M.S.K., Z.T.S. and A.N.J.; writing—original draft, M.S.K.; writing—review and editing, A.N.J. All authors have read and agreed to the published version of the manuscript.

**Funding:** This research was funded by the Nazarbayev University Collaborative Research Grant (grant number: 021220CRP1922), the Young Scientist Grant of the Ministry of Education and Science of the Republic of Kazakhstan (grant number: AP08052412), and the Scientific Research Grant from the Ministry of Education and Science of the Republic of Kazakhstan (grant number: AP08856931).

**Institutional Review Board Statement:** Not applicable.

**Informed Consent Statement:** Not applicable.

**Data Availability Statement:** The data presented in this study are available on request from the corresponding author.

**Acknowledgments:** We would like to thank the Core Facilities team of Nazarbayev University for their help and support with the measurements (Erzhigit Sugurbekov for the XRD measurements; Nikita Alexandrovich Lutchenko for the TEM measurements; Laura Khamkash and Nurgul Daniyeva for the SEM measurements). A.N.J. appreciates the Nazarbayev University Collaborative Research Grant (grant number: 021220CRP1922) and the Young Scientist Grant of the Ministry of Education and Science of the Republic of Kazakhstan (grant number: AP08052412). A.N. appreciates the Scientific Research Grant from the Ministry of Education and Science of the Republic of Kazakhstan (grant number: AP08856931).

**Conflicts of Interest:** The authors declare no conflict of interest.

## References

1. Ashina, A.; Battula, R.K.; Ramasamy, E.; Chundi, N.; Sakthivel, S.; Veerappan, G. Dip Coated SnO<sub>2</sub> Film as Electron Transport Layer for Low Temperature Processed Planar Perovskite Solar Cells. *Appl. Surf. Sci. Adv.* **2021**, *4*, 100066. [[CrossRef](#)]
2. Cao, J.-J.; Wang, K.-L.; Dong, C.; Li, X.-M.; Yang, W.-F.; Wang, Z.-K. Bottom-Contact Passivation for High-Performance Perovskite Solar Cells Using TaCl<sub>5</sub>-Doped SnO<sub>2</sub> as Electron-Transporting Layer. *Org. Electron.* **2021**, *88*, 105972. [[CrossRef](#)]
3. Jung, E.H.; Jeon, N.J.; Park, E.Y.; Moon, C.S.; Shin, T.J.; Yang, T.-Y.; Noh, J.H.; Seo, J. Efficient, Stable and Scalable Perovskite Solar Cells Using Poly(3-Hexylthiophene). *Nature* **2019**, *567*, 511–515. [[CrossRef](#)] [[PubMed](#)]
4. Razza, S.; Castro-Hermosa, S.; Di Carlo, A.; Brown, T.M. Research Update: Large-Area Deposition, Coating, Printing, and Processing Techniques for the Upscaling of Perovskite Solar Cell Technology. *APL Mater.* **2016**, *4*, 091508. [[CrossRef](#)]
5. Cai, B.; Zhang, W.-H.; Qiu, J. Solvent Engineering of Spin-Coating Solutions for Planar-Structured High-Efficiency Perovskite Solar Cells. *Chin. J. Catal.* **2015**, *36*, 1183–1190. [[CrossRef](#)]
6. Zhang, Z.; Wei, D.; Xie, B.; Yue, X.; Li, M.; Song, D.; Li, Y. High Reproducibility of Perovskite Solar Cells via a Complete Spin-Coating Sequential Solution Deposition Process. *Sol. Energy* **2015**, *122*, 97–103. [[CrossRef](#)]
7. Gong, C.; Tong, S.; Huang, K.; Li, H.; Huang, H.; Zhang, J.; Yang, J. Flexible Planar Heterojunction Perovskite Solar Cells Fabricated via Sequential Roll-to-Roll Microgravure Printing and Slot-Die Coating Deposition. *Sol. RRL* **2020**, *4*, 1900204. [[CrossRef](#)]
8. Zheng, J.; Zhang, M.; Lau, C.F.J.; Deng, X.; Kim, J.; Ma, Q.; Chen, C.; Green, M.A.; Huang, S.; Ho-Baillie, A.W.Y. Spin-Coating Free Fabrication for Highly Efficient Perovskite Solar Cells. *Sol. Energy Mater. Sol. Cells* **2017**, *168*, 165–171. [[CrossRef](#)]
9. Whitaker, J.B.; Hoe Kim, D.; Larson, B.W.; Zhang, F.; Berry, J.J.; van Hest, M.F.A.M.; Zhu, K. Scalable Slot-Die Coating of High Performance Perovskite Solar Cells. *Sustain. Energy Fuels* **2018**, *2*, 2442–2449. [[CrossRef](#)]
10. Sandström, A.; Dam, H.F.; Krebs, F.C.; Edman, L. Ambient Fabrication of Flexible and Large-Area Organic Light-Emitting Devices Using Slot-Die Coating. *Nat. Commun.* **2012**, *3*, 1002. [[CrossRef](#)]

11. Zhu, S.; Tian, J.; Zhang, J.; Gao, C.; Liu, X. Improving the Interfacial Contact of Screen-Printed Carbon Electrodes for Perovskite Solar Cells. *ACS Appl. Energy Mater.* **2021**, *4*, 5554–5559. [[CrossRef](#)]
12. Cao, K.; Zuo, Z.; Cui, J.; Shen, Y.; Moehl, T.; Zakeeruddin, S.M.; Grätzel, M.; Wang, M. Efficient Screen Printed Perovskite Solar Cells Based on Mesoscopic TiO<sub>2</sub>/Al<sub>2</sub>O<sub>3</sub>/NiO/Carbon Architecture. *Nano Energy* **2015**, *17*, 171–179. [[CrossRef](#)]
13. Yang, J.; Lim, E.L.; Tan, L.; Wei, Z. Ink Engineering in Blade-Coating Large-Area Perovskite Solar Cells. *Adv. Energy Mater.* **2022**, *12*, 2200975. [[CrossRef](#)]
14. Gao, B.; Meng, J. Flexible CH<sub>3</sub>NH<sub>3</sub>PbI<sub>3</sub> Perovskite Solar Cells with High Stability Based on All Inkjet Printing. *Sol. Energy* **2021**, *230*, 598–604. [[CrossRef](#)]
15. Gao, L.; Huang, K.; Long, C.; Zeng, F.; Liu, B.; Yang, J. Fully Slot-Die-Coated Perovskite Solar Cells in Ambient Condition. *Appl. Phys. A* **2020**, *126*, 452. [[CrossRef](#)]
16. Mathiazhagan, G.; Seeber, A.; Gengenbach, T.; Mastroianni, S.; Vak, D.; Chesman, A.S.R.; Gao, M.; Angmo, D.; Hinsch, A. Improving the Stability of Ambient Processed, SnO<sub>2</sub>-Based, Perovskite Solar Cells by the UV-Treatment of Sub-Cells. *Sol. RRL* **2020**, *4*, 2000262. [[CrossRef](#)]
17. Bahadur, J.; Ghahremani, A.H.; Martin, B.; Druffel, T.; Sunkara, M.K.; Pal, K. Solution Processed Mo Doped SnO<sub>2</sub> as an Effective ETL in the Fabrication of Low Temperature Planer Perovskite Solar Cell under Ambient Conditions. *Org. Electron.* **2019**, *67*, 159–167. [[CrossRef](#)]
18. Tzounis, L.; Stergiopoulos, T.; Zachariadis, A.; Gravalidis, C.; Laskarakis, A.; Logothetidis, S. Perovskite Solar Cells from Small Scale Spin Coating Process towards Roll-to-Roll Printing: Optical and Morphological Studies. *Mater. Today Proc.* **2017**, *4*, 5082–5089. [[CrossRef](#)]
19. Brunetti, F.; Operamolla, A.; Castro-Hermosa, S.; Lucarelli, G.; Manca, V.; Farinola, G.M.; Brown, T.M. Printed Solar Cells and Energy Storage Devices on Paper Substrates. *Adv. Funct. Mater.* **2019**, *29*, 1806798. [[CrossRef](#)]
20. Maafa, I.M. All-Inorganic Perovskite Solar Cells: Recent Advancements and Challenges. *Nanomaterials* **2022**, *12*, 1651. [[CrossRef](#)] [[PubMed](#)]
21. Afre, R.A.; Sharma, N.; Sharon, M.; Sharon, M. Transparent Conducting Oxide Films for Various Applications: A Review. *Rev. Adv. Mater. Sci.* **2018**, *53*, 79–89. [[CrossRef](#)]
22. Choi, Y.J.; Lee, H.Y.; Kim, S.; Song, P.K. Controlled Lattice Thermal Conductivity of Transparent Conductive Oxide Thin Film via Localized Vibration of Doping Atoms. *Nanomaterials* **2021**, *11*, 2363. [[CrossRef](#)] [[PubMed](#)]
23. Mohanraj, J.; Singh, C.R.; Gujar, T.P.; Heinrich, C.D.; Thelakkat, M. Nanostructured Hybrid Metal Mesh as Transparent Conducting Electrodes: Selection Criteria Verification in Perovskite Solar Cells. *Nanomaterials* **2021**, *11*, 1783. [[CrossRef](#)] [[PubMed](#)]
24. Zhu, N.; Qi, X.; Zhang, Y.; Liu, G.; Wu, C.; Wang, D.; Guo, X.; Luo, W.; Li, X.; Hu, H.; et al. High Efficiency (18.53%) of Flexible Perovskite Solar Cells via the Insertion of Potassium Chloride between SnO<sub>2</sub> and CH<sub>3</sub>NH<sub>3</sub>PbI<sub>3</sub> Layers. *ACS Appl. Energy Mater.* **2019**, *2*, 3676–3682. [[CrossRef](#)]
25. Rieu, M.; Camara, M.; Tournier, G.; Viricelle, J.-P.; Pijolat, C.; de Rooij, N.F.; Briand, D. Fully Inkjet Printed SnO<sub>2</sub> Gas Sensor on Plastic Substrate. *Sens. Actuators B Chem.* **2016**, *236*, 1091–1097. [[CrossRef](#)]
26. Dong, J.; Jia, J.; Feng, X.; Shi, B.; Wu, Y.; Zhang, Y.; Wu, J.; Cao, B. Ligand Exchange of SnO<sub>2</sub> Effectively Improving the Efficiency of Flexible Perovskite Solar Cells. *J. Alloys Compd.* **2021**, *883*, 160827. [[CrossRef](#)]
27. Wang, H.; Cao, S.; Yang, B.; Li, H.; Wang, M.; Hu, X.; Sun, K.; Zang, Z. NH<sub>4</sub>Cl-Modified ZnO for High-Performance CsPbIBr<sub>2</sub> Perovskite Solar Cells via Low-Temperature Process. *Sol. RRL* **2020**, *4*, 1900363. [[CrossRef](#)]
28. Liu, J.; He, X.; Li, X.; Li, Y. Solvent-Assisted Preparation of Low-Temperature SnO<sub>2</sub> Electron Transport Layers for Efficient and Stable Perovskite Solar Cells Made in Ambient Conditions. *New J. Chem.* **2022**, *46*, 9841–9850. [[CrossRef](#)]
29. Cao, Z.; Li, C.; Deng, X.; Wang, S.; Yuan, Y.; Chen, Y.; Wang, Z.; Liu, Y.; Ding, L.; Hao, F. Metal Oxide Alternatives for Efficient Electron Transport in Perovskite Solar Cells: Beyond TiO<sub>2</sub> and SnO<sub>2</sub>. *J. Mater. Chem. A* **2020**, *8*, 19768–19787. [[CrossRef](#)]
30. Lin, H.-K.; Li, J.-X.; Wang, H.-C.; Su, Y.-W.; Wu, K.-H.; Wei, K.-H. Dual Nanocomposite Carrier Transport Layers Enhance the Efficiency of Planar Perovskite Photovoltaics. *RSC Adv.* **2018**, *8*, 12526–12534. [[CrossRef](#)]
31. Wang, P.; Shao, Z.; Ulfa, M.; Pauporté, T. Insights into the Hole Blocking Layer Effect on the Perovskite Solar Cell Performance and Impedance Response. *J. Phys. Chem. C* **2017**, *121*, 9131–9141. [[CrossRef](#)]
32. Chen, Y.; Meng, Q.; Zhang, L.; Han, C.; Gao, H.; Zhang, Y.; Yan, H. SnO<sub>2</sub>-Based Electron Transporting Layer Materials for Perovskite Solar Cells: A Review of Recent Progress. *J. Energy Chem.* **2019**, *35*, 144–167. [[CrossRef](#)]
33. Shi, S.; Li, J.; Bu, T.; Yang, S.; Xiao, J.; Peng, Y.; Li, W.; Zhong, J.; Ku, Z.; Cheng, Y.-B.; et al. Room-Temperature Synthesized SnO<sub>2</sub> Electron Transport Layers for Efficient Perovskite Solar Cells. *RSC Adv.* **2019**, *9*, 9946–9950. [[CrossRef](#)] [[PubMed](#)]
34. Ai, Y.; Zhang, Y.; Song, J.; Kong, T.; Li, Y.; Xie, H.; Bi, D. In Situ Perovskitoid Engineering at SnO<sub>2</sub> Interface toward Highly Efficient and Stable Formamidinium Lead Triiodide Perovskite Solar Cells. *J. Phys. Chem. Lett.* **2021**, *12*, 10567–10573. [[CrossRef](#)] [[PubMed](#)]
35. Lu, D.; Zhang, W.; Kloos, L.; Belova, L. Inkjet-Printed Electron Transport Layers for Perovskite Solar Cells. *Materials* **2021**, *14*, 7525. [[CrossRef](#)]
36. Jiang, Y.; Sun, L.; Jiang, F.; Xie, C.; Hu, L.; Dong, X.; Qin, F.; Liu, T.; Hu, L.; Jiang, X.; et al. Photocatalytic Effect of ZnO on the Stability of Nonfullerene Acceptors and Its Mitigation by SnO<sub>2</sub> for Nonfullerene Organic Solar Cells. *Mater. Horiz.* **2019**, *6*, 1438–1443. [[CrossRef](#)]
37. Dkhissi, Y.; Huang, F.; Rubanov, S.; Xiao, M.; Bach, U.; Spiccia, L.; Caruso, R.A.; Cheng, Y.-B. Low Temperature Processing of Flexible Planar Perovskite Solar Cells with Efficiency over 10%. *J. Power Sources* **2015**, *278*, 325–331. [[CrossRef](#)]

38. Halvani Anaraki, E.; Kermanpur, A.; Steier, L.; Domanski, K.; Matsui, T.; Tress, W.; Saliba, M.; Abate, A.; Grätzel, M.; Hagfeldt, A.; et al. Highly Efficient and Stable Planar Perovskite Solar Cells by Solution-Processed Tin Oxide. *Energy Environ. Sci.* **2016**, *9*, 3128–3134. [CrossRef]
39. Ke, W.; Fang, G.; Liu, Q.; Xiong, L.; Qin, P.; Tao, H.; Wang, J.; Lei, H.; Li, B.; Wan, J.; et al. Low-Temperature Solution-Processed Tin Oxide as an Alternative Electron Transporting Layer for Efficient Perovskite Solar Cells. *J. Am. Chem. Soc.* **2015**, *137*, 6730–6733. [CrossRef]
40. Bu, T.; Li, J.; Zheng, F.; Chen, W.; Wen, X.; Ku, Z.; Peng, Y.; Zhong, J.; Cheng, Y.-B.; Huang, F. Universal Passivation Strategy to Slot-Die Printed SnO<sub>2</sub> for Hysteresis-Free Efficient Flexible Perovskite Solar Module. *Nat. Commun.* **2018**, *9*, 4609. [CrossRef]
41. Vijayaraghavan, S.N.; Wall, J.; Li, L.; Xing, G.; Zhang, Q.; Yan, F. Low-Temperature Processed Highly Efficient Hole Transport Layer Free Carbon-Based Planar Perovskite Solar Cells with SnO<sub>2</sub> Quantum Dot Electron Transport Layer. *Mater. Today Phys.* **2020**, *13*, 100204. [CrossRef]
42. Ren, Z.; Liu, K.; Hu, H.; Guo, X.; Gao, Y.; Fong, P.W.K.; Liang, Q.; Tang, H.; Huang, J.; Zhang, H.; et al. Room-Temperature Multiple Ligands-Tailored SnO<sub>2</sub> Quantum Dots Endow in Situ Dual-Interface Binding for Upscaling Efficient Perovskite Photovoltaics with High VOC. *Light Sci. Appl.* **2021**, *10*, 239. [CrossRef] [PubMed]
43. Sheikh, S.P.; Reddy, V.R.; Sen, P. Size-Dependent Nonlinear Optical Absorption in SnO<sub>2</sub> Quantum Dots. *J. Opt. Soc. Am. B* **2020**, *37*, 2788–2795. [CrossRef]
44. Tong, G.; Ono, L.K.; Liu, Y.; Zhang, H.; Bu, T.; Qi, Y. Up-Scalable Fabrication of SnO<sub>2</sub> with Multifunctional Interface for High Performance Perovskite Solar Modules. *Nano-Micro Lett.* **2021**, *13*, 155. [CrossRef] [PubMed]
45. Zhang, J.; Zhang, W.; Cheng, H.-M.; Silva, S.R.P. Critical Review of Recent Progress of Flexible Perovskite Solar Cells. *Mater. Today* **2020**, *39*, 66–88. [CrossRef]
46. Ahsan Saeed, M.; Hyeon Kim, S.; Baek, K.; Hyun, J.K.; Youn Lee, S.; Won Shim, J. PEDOT:PSS: CuNW-Based Transparent Composite Electrodes for High-Performance and Flexible Organic Photovoltaics under Indoor Lighting. *Appl. Surf. Sci.* **2021**, *567*, 150852. [CrossRef]
47. Liu, J.; Xue, W.; Jin, G.; Zhai, Z.; Lv, J.; Hong, W.; Chen, Y. Preparation of Tin Oxide Quantum Dots in Aqueous Solution and Applications in Semiconductor Gas Sensors. *Nanomaterials* **2019**, *9*, 240. [CrossRef]
48. Zhu, H.; Yang, D.; Yu, G.; Zhang, H.; Yao, K. A Simple Hydrothermal Route for Synthesizing SnO<sub>2</sub> quantum Dots. *Nanotechnology* **2006**, *17*, 2386–2389. [CrossRef]
49. Hussain, I.; Tran, H.P.; Jaksik, J.; Moore, J.; Islam, N.; Uddin, M.J. Functional Materials, Device Architecture, and Flexibility of Perovskite Solar Cell. *Emergent Mater.* **2018**, *1*, 133–154. [CrossRef]
50. Lu, C.; Zhang, W.; Jiang, Z.; Zhang, Y.; Ni, C. CuI/Spiro-OMeTAD Double-Layer Hole Transport Layer to Improve Photovoltaic Performance of Perovskite Solar Cells. *Coatings* **2021**, *11*, 978. [CrossRef]
51. Chen, W.; Zhou, Q.; Wan, F.; Gao, T. Gas Sensing Properties and Mechanism of Nano-SnO<sub>2</sub>-Based Sensor for Hydrogen and Carbon Monoxide. *J. Nanomater.* **2012**, *2012*, 612420. [CrossRef]
52. Lamdhade, G.T.; Raghuwanshi, F.C.; Agrawal, R.M.; Balkhande, V.M.; Shripath, T. SnO<sub>2</sub> Nanoparticles Synthesis Via Liquid-Phase Co-Precipitation Technique. *Adv. Mater. Lett.* **2015**, *6*, 738–742. [CrossRef]
53. Rani, R.; Sharma, S. Preparation and Characterization of SnO<sub>2</sub> Nanofibers via Electrospinning. *Adv. Nanoparticles* **2016**, *5*, 53–59. [CrossRef]
54. Bhattacharjee, A.; Ahmaruzzaman, M. A Novel and Green Process for the Production of Tin Oxide Quantum Dots and Its Application as a Photocatalyst for the Degradation of Dyes from Aqueous Phase. *J. Colloid Interface Sci.* **2015**, *448*, 130–139. [CrossRef]
55. Xie, J.; Huang, K.; Yu, X.; Yang, Z.; Xiao, K.; Qiang, Y.; Zhu, X.; Xu, L.; Wang, P.; Cui, C.; et al. Enhanced Electronic Properties of SnO<sub>2</sub> via Electron Transfer from Graphene Quantum Dots for Efficient Perovskite Solar Cells. *ACS Nano* **2017**, *11*, 9176–9182. [CrossRef]
56. Ou, X.-L.; Feng, J.; Xu, M.; Sun, H.-B. Semitransparent and Flexible Perovskite Solar Cell with High Visible Transmittance Based on Ultrathin Metallic Electrodes. *Opt. Lett.* **2017**, *42*, 1958–1961. [CrossRef]
57. Remarkably High Performance of Organic Photovoltaic Devices with 3,9-Bis(2-Methylene-(3-(1,1-Dicyanomethylene)-Indanone))-5,5,11,11-Tetrakis(4-Hexyl Meta-Phenyl)-Dithieno[2,3-d:2',3'-d']-s-Indaceno[1,2-b:5,6-b']Dithiophene- Ethylhexyloxy] Photoactive Acceptor under Halogen Light Illumination-ScienceDirect. Available online: <https://www.sciencedirect.com/science/article/pii/S0378775321012738> (accessed on 30 June 2022).
58. Elastomeric Indoor Organic Photovoltaics with Superb Photothermal Endurance-Kim-Advanced Functional Materials-Wiley Online Library. Available online: <https://onlinelibrary.wiley.com/doi/abs/10.1002/adfm.202201921> (accessed on 30 June 2022).
59. Jeyakumar, R.; Bag, A.; Nekovei, R.; Radhakrishnan, R. Influence of Electron Transport Layer (TiO<sub>2</sub>) Thickness and Its Doping Density on the Performance of CH<sub>3</sub>NH<sub>3</sub>PbI<sub>3</sub>-Based Planar Perovskite Solar Cells. *J. Electron. Mater.* **2020**, *49*, 3533–3539. [CrossRef]
60. Impact of Interfacial Layers in Perovskite Solar Cells-Cho-2017-ChemSusChem-Wiley Online Library. Available online: <https://chemistry-europe.onlinelibrary.wiley.com/doi/full/10.1002/cssc.201701095> (accessed on 31 May 2022).
61. Habisreutinger, S.N.; Noel, N.K.; Snaith, H.J. Hysteresis Index: A Figure without Merit for Quantifying Hysteresis in Perovskite Solar Cells. *ACS Energy Lett.* **2018**, *3*, 2472–2476. [CrossRef]

62. Cao, Q.; Li, Y.; Zhang, H.; Yang, J.; Han, J.; Xu, T.; Wang, S.; Wang, Z.; Gao, B.; Zhao, J.; et al. Efficient and Stable Inverted Perovskite Solar Cells with Very High Fill Factors via Incorporation of Star-Shaped Polymer. *Sci. Adv.* **2021**, *7*, eabg0633. [CrossRef]
63. Rai, M.; Wong, L.H.; Etgar, L. Effect of Perovskite Thickness on Electroluminescence and Solar Cell Conversion Efficiency. *J. Phys. Chem. Lett.* **2020**, *11*, 8189–8194. [CrossRef]
64. Tan, H.; Jain, A.; Voznyy, O.; Lan, X.; García de Arquer, F.P.; Fan, J.Z.; Quintero-Bermudez, R.; Yuan, M.; Zhang, B.; Zhao, Y.; et al. Efficient and Stable Solution-Processed Planar Perovskite Solar Cells via Contact Passivation. *Science* **2017**, *355*, 722–726. [CrossRef] [PubMed]
65. Weber, S.; Rath, T.; Mangalam, J.; Kunert, B.; Coclite, A.M.; Bauch, M.; Dimopoulos, T.; Trimmel, G. Investigation of NiOx-Hole Transport Layers in Triple Cation Perovskite Solar Cells. *J. Mater. Sci. Mater. Electron.* **2018**, *29*, 1847–1855. [CrossRef]
66. Bush, K.A.; Bailie, C.D.; Chen, Y.; Bowring, A.R.; Wang, W.; Ma, W.; Leijtens, T.; Moghadam, F.; McGehee, M.D. Thermal and Environmental Stability of Semi-Transparent Perovskite Solar Cells for Tandems Enabled by a Solution-Processed Nanoparticle Buffer Layer and Sputtered ITO Electrode. *Adv. Mater.* **2016**, *28*, 3937–3943. [CrossRef]
67. Hoang, V.Q.; Lee, S.K.; Bark, C.W. Dispersed SnO<sub>2</sub> Colloids Using Sodium Dodecyl Benzene Sulfonate for High-Performance Planar Perovskite Solar Cells. *Sol. Energy* **2021**, *230*, 747–753. [CrossRef]
68. Chander, S.; Purohit, A.; Nehra, A.; Nehra, S.P.; Dhaka, M.S. A Study on Spectral Response and External Quantum Efficiency of Mono-Crystalline Silicon Solar Cell. *Int. J. Renew. Energy Res.* **2015**, *4*, 41–44.
69. Slami, A.; Benramdane, N. Manual Method for Measuring The External Quantum Efficiency for Solar Cells. *E3S Web Conf.* **2021**, *229*, 01005. [CrossRef]
70. Jo Kim, B.; Hoe Kim, D.; Lee, Y.-Y.; Shin, H.-W.; Sang Han, G.; Sug Hong, J.; Mahmood, K.; Kyu Ahn, T.; Joo, Y.-C.; Sun Hong, K.; et al. Highly Efficient and Bending Durable Perovskite Solar Cells: Toward a Wearable Power Source. *Energy Environ. Sci.* **2015**, *8*, 916–921. [CrossRef]
71. Wang, C.; Guan, L.; Zhao, D.; Yu, Y.; Grice, C.R.; Song, Z.; Awni, R.A.; Chen, J.; Wang, J.; Zhao, X.; et al. Water Vapor Treatment of Low-Temperature Deposited SnO<sub>2</sub> Electron Selective Layers for Efficient Flexible Perovskite Solar Cells. *ACS Energy Lett.* **2017**, *2*, 2118–2124. [CrossRef]
72. Yang, F.; Liu, J.; Lim, H.E.; Ishikura, Y.; Shinokita, K.; Miyauchi, Y.; Wakamiya, A.; Murata, Y.; Matsuda, K. High Bending Durability of Efficient Flexible Perovskite Solar Cells Using Metal Oxide Electron Transport Layer. *J. Phys. Chem. C* **2018**, *122*, 17088–17095. Available online: <https://pubs.acs.org/doi/10.1021/acs.jpcc.8b05008> (accessed on 12 July 2022). [CrossRef]
73. Heo, J.H.; Shin, D.H.; Jang, M.H.; Lee, M.L.; Kang, M.G.; Im, S.H. Highly Flexible, High-Performance Perovskite Solar Cells with Adhesion Promoted AuCl<sub>3</sub>-Doped Graphene Electrodes. *J. Mater. Chem. A* **2017**, *5*, 21146–21152. [CrossRef]
74. Popoola, I.K.; Gondal, M.A.; Qahtan, T.F. Recent Progress in Flexible Perovskite Solar Cells: Materials, Mechanical Tolerance and Stability. *Renew. Sustain. Energy Rev.* **2018**, *82*, 3127–3151. [CrossRef]
75. Xu, Y.; Lin, Z.; Wei, W.; Hao, Y.; Liu, S.; Ouyang, J.; Chang, J. Recent Progress of Electrode Materials for Flexible Perovskite Solar Cells. *Nano-Micro Lett.* **2022**, *14*, 117. [CrossRef] [PubMed]
76. Flexible Perovskite Solar Cells with Simultaneously Improved Efficiency, Operational Stability, and Mechanical Reliability-ScienceDirect. Available online: <https://www.sciencedirect.com/science/article/pii/S2542435121002002?via%3Dihub> (accessed on 12 July 2022).
77. Record Efficiency Stable Flexible Perovskite Solar Cell Using Effective Additive Assistant Strategy-Feng-2018-Advanced Materials-Wiley Online Library. Available online: <https://onlinelibrary.wiley.com/doi/full/10.1002/adma.201801418> (accessed on 12 July 2022).
78. Lee, G.; Kim, M.; Choi, Y.W.; Ahn, N.; Jang, J.; Yoon, J.; Kim, S.M.; Lee, J.-G.; Kang, D.; Jung, H.S.; et al. Ultra-Flexible Perovskite Solar Cells with Crumpling Durability: Toward a Wearable Power Source. *Energy Environ. Sci.* **2019**, *12*, 3182–3191. [CrossRef]
79. Cheacharoen, R.; Rolston, N.; Harwood, D.; Bush, K.A.; Dauskardt, R.H.; McGehee, M.D. Design and Understanding of Encapsulated Perovskite Solar Cells to Withstand Temperature Cycling. *Energy Environ. Sci.* **2018**, *11*, 144–150. [CrossRef]
80. Jiang, N.R.; Wang, Y.F.; Dong, Q.F.; Ge, C.D.; Yang, Z.Q.; Yin, D. Enhanced Efficiency and Mechanical Robustness of Flexible Perovskite Solar Cells by Using HPbI<sub>3</sub> Additive. *Sol. RRL* **2021**, *5*, 2000821. Available online: <https://onlinelibrary.wiley.com/doi/abs/10.1002/solr.202000821> (accessed on 12 July 2022). [CrossRef]
81. Impact of Interlayer Application on Band Bending for Improved Electron Extraction for Efficient Flexible Perovskite Mini-Modules-ScienceDirect. Available online: <https://www.sciencedirect.com/science/article/pii/S2211285518302866?via%3Dihub> (accessed on 12 July 2022).
82. Sears, K.K.; Fievez, M.; Gao, M.; Weerasinghe, H.C.; Easton, C.D.; Vak, D. ITO-Free Flexible Perovskite Solar Cells Based on Roll-to-Roll, Slot-Die Coated Silver Nanowire Electrodes. *Sol. RRL* **2017**, *9*, 1700059. [CrossRef]
83. Patterson, A.L. The Scherrer Formula for X-Ray Particle Size Determination. *Phys. Rev.* **1939**, *56*, 978–982. [CrossRef]
84. Bokuniaeva, A.O.; Vorokh, A.S. Estimation of Particle Size Using the Debye Equation and the Scherrer Formula for Polyphasic TiO<sub>2</sub> Powder. *J. Phys.* **2019**, *1410*, 012057. [CrossRef]